Integrated hydrostratigraphic interpretation of 3D seismic reflection and multi-fold, pseudo 3D GPR data

John H. Bradford
Center for Geophysical Investigation of the Shallow Subsurface
Boise State University
Boise, Idaho, USA
(208) 426-3898
johnb@cgiss.boisestate.edu

ABSTRACT

To map the 3D distribution of major hydrologic boundaries in a shallow aquifer near Boise, Idaho, I analyzed 3D seismic reflection and multi-fold, pseudo 3D GPR data. The seismic data covered a 75 m x 70 m area and imaged horizons from 18 – 150 m depth. The 10-fold, 50 MHz GPR data were acquired on a 20 m x 30 m grid with a multi-channel GPR system and offsets ranging from 2 m – 20 m. By correlating the well resolved GPR depth image with a clay aquitard seismic reflection, I was able to substantially improve the seismic velocity model and the accuracy of the final interpretation. The resulting clay aquitard surface differed from the depth-to-clay measured in wells by 0.12 ± 0.46 m. By integrating the interpretation of the GPR and seismic data, I was able to produce a 3D map of major hydrostratigraphic boundaries.

INTRODUCTION

It is useful to think of the similarities and differences between electromagnetic (EM) and elastic waves in terms of kinematics and dynamics. The dynamics describe the mechanisms of a physical interaction and clearly we cannot draw dynamic analogies between EM and elastic waves. The kinematics of a system describe the changes in time without regard to the physical mechanisms. It is through the kinematics that we can find similarities between all types of wave propagation and find mathematical analogies. Indeed several authors have used a unified mathematical framework to describe elastic and EM wave propagation (Szaraneic, 1976; Szaraneic, 1979; Ursin, 1983). Because of the kinematic analogy between ground-penetrating radar (GPR) and seismic techniques, many of the processing tools and interpretation techniques we use to analyze the data are often similar or the same.

In conventional reflection imaging, reflected waves are recorded at the surface and used to produce a 2D or 3D reflector map of the subsurface. The reflector map indicates the location of subsurface property contrasts. Seismic reflections are generated at acoustic impedance contrasts (product of density and velocity) while GPR reflections are primarily a function of dielectric permittivity and electric conductivity contrasts (magnetic permeability also plays a role but is approximately constant in many applications). Often, elastic and dielectric contrasts are coincident. For example, in a thorough petrophysical study of a low water-content sandstone, Koesoemadinata and McMechan (2002) found an imperfect, but positive correlation ($R^2 = 0.55$) between dielectric permittivity and compressional wave velocity. Because of this relationship, GPR reflection and seismic reflection images provide complementary information that sometimes reveal the same boundaries. The equivalent boundaries can then be used to integrate seismic and GPR datasets and may help improve the overall interpretation.

Seismic and GPR reflector maps are subject to the resolution limits of the data and scale differences can complicate interpretation and data integration. For both seismic and GPR, the resolution limit is often taken as ¼ of the wavelength at the dominant frequency of the reflected wavelet: two boundaries must be vertically separated by greater than this amount for the adjacent wavelet peaks or troughs to be differentiated in the reflection image. GPR operates in the $10^7 – 10^9$ Hz range while seismic operates in the 10 – 1000 Hz range. Similarly, GPR velocities are on the order of 10^8 m/s and seismic velocities are on the order of 10^3 m/s. While the magnitude of GPR and seismic frequencies and velocity differ by five to six orders of magnitude, the ratios scale proportionally and seismic and GPR wavelengths are often of the same order. Consider a seismic signal with a dominate frequency of 200 Hz, and a 50 MHz GPR signal. In a typical unsaturated sand, both the seismic and GPR wavelengths are about 2 m. Once the sand is saturated, the seismic velocity increases by a factor of about 5, while the EM velocity decreases by a factor of about 2 and the respective wavelengths become 10 m and 1 m. The resolution potential of each method can vary dramatically and differently within a given survey and this possibility must be considered when jointly interpreting coincident datasets. Table 1 lists ranges of compressional wave and electromagnetic velocities and a comparison of wavelengths for typical near surface studies.

Given the similarities and complementary information provided by GPR and seismic reflection methods, it may be surprising that the two methods are not often used together for site investigation. To understand this we can go back to the dynamics of the wave propagation. Seismic waves are most efficiently generated and recorded where cohesive materials are found at the surface. In unconsolidated sediments, this means moist, fine grained material. GPR signals are strongly attenuated by electrically conductive material and therefore propagate most

efficiently through dry coarse grained material. Therefore, the ideal conditions for the two methods are in very different environments.

Despite the differences in "ideal" conditions for seismic and GPR methods, there is a substantial region of overlap in suitable material types so that in some cases both tools may be deployed effectively and a number of studies have exploited this overlap to investigate joint analysis and improve interpretation for applications ranging from neotectonic characterization of faults to hydrogeophysical and waterborne applications.

In one of the first published studies of coincident GPR and seismic reflection data, Cardimona et al. (1998) imaged the top of a 10- 15 m deep aquitard at the base of a shallow unconfined aquifer. A shallow clay lense prevented GPR signal penetration to the aquitard at some locations but the complimentary information provided by the two data sets substantially improved interpretation.

Baker et al. (2001) acquired an ultrashallow (< 3m) seismic reflection survey using a .22 caliber rifle source that produced a signal with a 400 MHz dominant frequency. Sediments at the site consisted of medium and course grained sand and gravel. Multiple horizons in the seismic data were coincident with horizons imaged using a 225 MHz GPR system. The somewhat higher resolution of the GPR signal provided greater detail in the interpretation. However, due to a diffuse transition from unsaturated to saturated conditions, a GPR reflection was not generated at the water table, whereas this horizon was clearly delineated in the seismic image.

Bachrach and Rickett (1999) acquired a similarly high resolution (dominant frequency 300 Hz) seismic dataset and were able to correlate reflections with 100 MHz GPR data above the water table. In this case both methods imaged the water table. Bachrach and Rickett noted difficulty in interpreting some details of the images because of the change in support volume of

GPR and seismic measurements caused by opposite and substantial changes in EM and seismic wavelengths in response to water content variation. This study highlights the need to consider scaling issues when integrating seismic and GPR measurements.

Sloan et al. (2007) merged 190 Hz seismic reflection and 75 MHz GPR datasets by summing in the depth domain. This approach provided a single coherent reflection section. The GPR data provided a high resolution image of the unsaturated zone (< 6 m) while the seismic data imaged deeper stratigraphic features as well as bedrock at a depth of approximately 30 m. Since the radar signal only penetrated to the water table and the wavelengths of the seismic and GPR signals were similar in the vadose zone, summation worked well. As noted by the authors, because of the opposite change in wavelengths, summation would not have been effective for radar reflectors in the saturated zone. Rashed and Nakagawa (2004) and Chow et al. (2001) also supplemented deeper seismic images by using GPR for high resolution imaging of the upper few meters in studies of active faults.

In fresh water environments GPR can be effective for imaging subbottom stratigraphy. Typically, seismic signals can be generated and recorded in the marine environment at an order of magnitude higher than on land. Because of this, where GPR and seismic data can be coincidently acquired in a waterborne environment, a similar scale of resolution may be maintained. This similarity is illustrated by Haeni (1996) who summarizes coincident seismic and GPR case studies from pond and river environments. Schwamborn et al. (2002) describe the study of a lake in Northern Siberia where seismic subbottom images were acquired in up to 13 m of open water and coincident GPR images were acquired in the winter when the surface of the lake was frozen. It should also be noted that in addition to subbottom imaging, both acoustic and

GPR methods can be used to image thermal stratigraphy and other features within the water column (Bradford et al., 2007; Imberger, 1985; Thorpe and Brubaker, 1983).

All of the studies mentioned above utilized qualitative comparisons of seismic and GPR reflections, however, quantitative, coupled, analysis of the two types of data can lead to improved estimates of material properties. Ghose and Slob (2006) show that by using a common earth model to formulate the solution for both seismic and GPR analysis, joint inversion of offset dependent reflectivity curves can produce a unique solution for water saturation and porosity.

For completeness, I mention here the seismo-electric effect which provides a different sort of symmetry between elastic waves and electromagnetic fields. It is now well established that a propagating elastic wave causes a temporary charge dislocation in subsurface materials and this charge dislocation produces an electromagnetic field that can be measured. The symmetry arises as charge dislocation caused by a propagating electric field produces a mechanical disturbance that can be measured as a seismic wave. The electromagnetic field produced by the seismo-electric effect is in the same frequency range as the seismic signal that generated it (10^0-10^2 Hz for a typical surface study). This is well below the electromagnetic wave propagation regime of GPR (10^6-10^9 Hz) but this low frequency electric field can also be used to image boundaries in common with GPR. Dupois et al. (2007) give an excellent example of a horizon imaged by both the seismo-electric field and GPR.

In this study, I present the results of coincident 3D seismic reflection and pseudo-3D multi-fold GPR imaging in the study of an aquifer system located near Boise, Idaho. The primary objective of the work was imaging the upper surface of a clay aquitard at a depth of ~20 m and identifying significant stratigraphic horizons beneath the aquitard that may have hydrologic significance. The dry, coarse-grained, surface sediments at the site are ideal for GPR

data acquisition. However, the environment, at first glance, appears ill suited to the surface seismic reflection method. Despite this apparent adversity, a shallow water table enabled acquisition of high quality seismic data. I take advantage of the high resolution afforded by the GPR data and a common seismic and GPR horizon to improve the seismic velocity model. I then combine the interpretation of both datasets to produce a 3D image of significant hydrostratigraphic horizons.

FIELD DATA ACQUISITION AND PROCESSING

Site Description

Data for this study were acquired as part of an ongoing effort to characterize the Boise Hydrogeophysical Research Site (BHRS). The BHRS is an experimental well field located on a gravel bar adjacent to the Boise River 15 km from downtown Boise, Idaho (Barrash et al., 1999) (Figure 1). The surface aquifer is comprised of the youngest in a series of Pleistocene to Holocene coarse fluvial deposits that mantle a sequence of successively older and higher terraces. Core surveys at the BHRS show coarse, unconsolidated and unaltered fluvial deposits underlain by a red clay at a depth of 18 – 20 m below the surface (Barrash and Clemo, 2002; Barrash and Reboulet, 2004). Analogous deposits that are exposed in the Boise area show massive coarse-gravel sheets; sheets with weak subhorizontal layering and with planar and trough-cross-bedded coarse-gravel facies; and sand channels, lenses and drapes which are similar to classic deposits such as the Rhine gravels (Heinz et al., 2003; Jussel et al., 1994; Klingbeil et al., 1999) .

The central well field (~ 20 m diameter) is comprised of 13 wells in two concentric rings of six wells each around a central well (Barrash et al., 1999). Additionally, there are five boundary wells ~ 10 – 35 m from the central area (Figure 1). This design has supported a wide

variety of borehole-based hydrologic and geophysical tests and analysis (Barrash et al., 2006; Cardiff et al., 2009; Clement et al., 2006; Clement and Knoll, 2006; Ernst et al., 2007; Irving et al., 2007; Jardani et al., 2009; Johnson et al., 2007; Moret et al., 2006; Mwenifumbo et al., 2009). The saturated thickness of the shallow, unconfined aquifer at the BHRS ranges between 16 and 18 m depending on seasonal variation in river stage. Similarly the vadose zone above the aquifer varies from < 1 m to 2.5 m depending on surface topography and river stage.

The stratigraphy of the shallow unconfined aquifer is comprised of five distinct units based on stratigraphic position in the sediment column and differentiation by porosity and lithology (Figure 2; Barrash and Clemo, 2002; Barrash and Reboulet, 2004). The major characteristics of each unit are listed in Table 2.

In a 3D multi-fold GPR study, Bradford et al. (2009) derived a 3D GPR velocity volume for the central BHRS using reflection tomography. They showed that the surface derived velocities agreed with velocities determined from 1D inversion (Clement and Knoll, 2006) of vertical radar profiles (VRP) to within 2% when averaged over a few wavelengths. Bradford et al. (2009) went on to estimate the porosity distribution using the CRIM equation (Wharton et al., 1980) and found that the GPR estimated porosities agreed with neutron porosity log measurements to within 8% of the mean porosity. With the exception of the Unit 2/Unit 3 transition, the porosity contrasts across unit boundaries result in dielectric permittivity contrasts that generate well-defined radar reflectors observed in surface GPR profiles (Barrash and Clemo, 2002; Barrash and Reboulet, 2004; Bradford et al., 2009; Clement et al., 2006). The transition from Unit 2 to Unit 3 is irregular and gradational and does not generate a distinct GPR reflection.

Borehole seismic data have also proven useful at the BHRS. Using 1D inversion of vertical seismic profiles (VSP), Moret et al. (2004) showed that compressional seismic slowness

values have a strong correlation with porosity in the unconfined aquifer. Prior to the present exposition, no surface seismic reflection data at the site have been published.

While the unconfined aquifer is well characterized, little is known about the system below the shallow clay aquitard, nor is the surface of the aquitard well constrained outside of the central wellfield. The Boise State hydrogeophysical research group has an interest in extending the experimental well field laterally as well as deeper into the underlying confined aquifer. The purpose of the present study is to map the clay aquitard over the entire well field and to identify and map the distribution of major units in the underlying confined aquifer system.

GPR Data

Acquisition. The GPR survey was designed to image the central well field and covered an area of 20 x 30 m (Figure 1). A Sensors and Software PulseEKKO Pro system, with multi-channel adapter, 1000 V transmitter, and 50 MHz antennas was utilized to acquire multifold data along five in-line (Y direction) profiles and 11 cross-line (X direction) profiles. Data were acquired in 3 passes in an off-end geometry with 1 transmitter and 4 receivers for the first 2 passes and 1 transmitter with 2 receivers for the final pass. Offsets varied from 2 m to 20 m with 2 m spacing between receivers. The antennas were attached to wheeled carts and the entire system was towed by hand. Traces were acquired every 15 cm with position control maintained by an odometer wheel trigger and 16 traces were vertically stacked on each trigger. Because of surface obstructions including well casings, trees, and bushes, it was not possible to avoid spatial aliasing between profiles; spacing between lines varied from 2 to 6 m. Because of spatial aliasing between lines, true 3D processing was not possible and therefore I term this a pseudo-3D survey.

Acquisition of these data was coincident with, and utilized the same GPR system as the 100 MHz 3D survey described by Bradford et al. (2009). The 100 MHz survey provided a 3D image of the major stratigraphic boundaries to a depth of 15 m (Units 2-5) but failed to image the aquifer/aquitard boundary at a depth of 18 – 20 m. Imaging this clay surface was the primary objective for the 50 MHz survey.

Processing. Data pre-processing consisted of 1) 3D binning onto a 0.5 x 0.5 m CMP binning grid, 2) channel dependent time-zero correction as described by Bradford et al. (2009), 3) bandpass filter (6-12-60-120 MHz) to attenuate the low frequency transient and high frequency random noise, and 4) automatic gain control with a 40 ns window. After this processing stream, common-midpoint gathers show coherent reflections over the full range of offsets throughout the survey area (Figure 3). The deepest reflection is from the clay aquitard and has a near offset arrival time of approximately 450 ns.

While the clay reflection is evident in the CMP gathers, it is almost totally obscured by surface scatter in a conventional single offset GPR image (Figure 4A). The clarity of this reflection is significantly enhanced simply by NMO correcting and stacking the data (Figure 4B). To further enhance the subsurface reflections, I applied an NMO correction at air velocity in the CMP domain. After this correction, surface scattered events had infinite apparent velocity while subsurface reflections maintained positive residual moveout. I used an *f-k* filter to attenuate events with infinite apparent velocity and followed this with an inverse NMO correction at air velocity. These *f-k* filtered data were then NMO corrected and stacked at the subsurface velocity. This procedure effectively eliminates the surface scatter and has minimal impact on the subsurface reflectors. In the final CMP stack, the surface scatter is strongly attenuated and the clay reflection is revealed throughout the survey area (Figure 4C).

To derive a depth velocity model, I used the reflection tomography method of Stork (1992) to invert for velocity along all profiles oriented in the inline (Y) direction (Figure 1). This orientation is approximately perpendicular to the prominent dip of the Unit 4-Unit 5 stratigraphic boundary in which case the 2D velocity model assumption is reasonable. For the starting velocity model, I utilized the velocity model previously derived by Bradford et al. (2009). The Unit 1 velocity was not constrained by the earlier 100 MHz survey because the 100 MHz signal did not reach the clay aquitard. I inverted for the Unit 1 velocity while holding the velocity constant in the region above the Unit 2/Unit 1 boundary. The final GPR data volume is a CMP stack that is depth converted using the tomographic depth velocity model (Figure 5). This new velocity model now forms a complete picture of the shallow aquifer and correlates with the distribution of Units 1 – 5 (Figures 2 and 5). Note that while the Unit 2/Unit 3 boundary does not produce a coherent reflection, it is possible to map all five units based on the GPR velocity distribution alone (Figures 2 and 5).

Seismic Data

Acquisition. The seismic survey grid was deployed to span the outer ring of wells with dimensions of approximately 75 x 70 m (Figure 1). The acquisition system consisted of 4, 60 channel seismographs recording separately, but with a common trigger cable. Receivers consisted of single, 40 Hz geophones planted on a 5 x 5 m grid with 15 stations in the inline (Y) direction and 16 stations in the cross line (X) direction. The receiver grid was held static while shooting through the source grid. Spatial density was increased by locating source points on a 2.5 x 2.5 m grid. The source was an 8 kg sledge hammer on a steel plate with 8 hammer blows vertically stacked at each shot location. The acquisition procedure resulted in good data quality

with the reflection from the clay aquitard present at a near offset travel time of 30 – 40 ms as well as a series of deeper reflections at traveltimes up to 180 ms (Figure 6).

Processing. For CMP processing I binned the data onto a 1.25 x 1.25 m CMP grid. This resulted in a maximum CMP fold of 240 and average fold of 55, with the highest coverage near the central portion of the wellfield (Figure 7). I applied a conventional data processing scheme to the data that consisted of 1) time variant band-pass filter that varied from 100-200-500-1000 Hz at 50 ms to 60-120-500-1000 Hz at 80 ms and greater, 2) automatic gain control (50 ms time gate), 3) elevation and residual statics (described in greater detail below), 4) NMO velocity analysis, 5) inside and top muting to remove the noise cone and first arrival refraction respectively, and 6) CMP stacking and depth conversion.

A 2 m high sand berm on the northeastern side of the site (Figure 1) resulted in substantial statics anomalies (Figure 6A) and the application of residual statics was particularly important. The residual statics procedure consisted of an initial NMO velocity analysis and moveout correction followed by residual statics calculation using a modified form of the surface consistent, stack-power maximization algorithm described by Ronen and Claerbout (1985). After application of residual statics, NMO velocity analysis was repeated to produce the final stacking velocity model. The shot records after static corrections show a substantial improvement in reflector coherence (Figure 6B) and this improvement in coherence led to high quality CMP gathers for velocity analysis (Figure 8) with the dominant frequency of the reflections controlled by the low shoulder of the bandpass filter (200 Hz for shallow reflections grading to 120 Hz for reflections at 80 ms or greater). The importance of statics is evident in the in-line stack slices which cross the sand berm (Figure 9). Prior to residual statics, the clay aquitard reflection is poorly imaged below the sand berm (Figure 9A) whereas after statics the

reflection is coherent throughout the data volume and the coherence of deeper reflections is substantially improved (Figure 9B).

To determine the seismic interval velocity model I first modified the stacking velocity functions to include the low velocity surface layer. I picked the traveltime of the direct arrival from 20 shot records distributed throughout the survey, then fit a line to all the picks and found a velocity of 495 m/s ± 18 m/s. I computed the mean two-way traveltime to the water table (8ms) based on the mean water table depth of 2 m measured in the wells, and then inserted the velocity of 495 m/s into the stacking velocity functions. Finally, I computed the interval velocity model using Dix inversion (Figure 10), and used this interval velocity model to depth convert the stacked data.

DATA INTEGRATION AND INTERPRETATION

Improving the seismic velocity model

With stacked, depth-converted data volumes complete, I picked the clay aquitard reflection in the seismic and GPR data. I first picked the central peak of the reflection, then shifted the picks upward so that the horizon would correspond to the first motion of the reflected wavelet; the true position of the reflecting boundary. The upward shift was 4 m for the seismic data and 1 m for the GPR data. Subtracting these initial clay horizon picks from the clay depths measured in well data I found that the difference was 1.5 ± 0.5 m for the seismic horizon and 0.03 ± 0.32 m for the GPR horizon. Relative to the dominant signal wavelengths (12 m for seismic, 2.8 m for GPR) these estimates are remarkably accurate. However, the difference in the seismic horizon is greater than the uncertainty suggesting that there may be some bias in the result.

In the saturated zone above the aquitard, the initial seismic interval velocity estimate was 2155 m/s**.** This value is 10.6 % lower than the mean value of 2400 m/s determined by Moret et al. (2004) from VSP analysis. The underestimate of the interval velocity explains the initial underestimate of clay depth. The noise cone and first arrival refraction limit the offset aperture available for velocity analysis to between 18 and 35 m, and this small offset aperture limits the accuracy of the stacking velocity measurement.

To test how well I could improve the seismic velocity model and clay depth estimate using only information derived from the seismic reflection and GPR data, I first computed the mean difference between the seismic and GPR clay horizons (1.4 ± 0.3 m). I then computed the mean change in seismic rms velocity that would be required to shift the seismic clay horizon downward by 1.4 m and added this value to my stacking velocity functions. Finally, I used these updated velocity functions to compute a new interval velocity function (Figure 10). The updated mean interval velocity in the shallow aquifer is 2417 m/s which is in good agreement with Moret et al.'s (2004) VSP determined value of 2400 m/s. After updating the velocity model, the difference between seismic and GPR clay horizons is 0.05 ± 0.31 m, and the difference between the seismic clay horizon and clay depths measured in wells is 0.12 ± 0.46 m. In both of these comparisons, the mean difference is now substantially less than the variability indicating the bias in the seismic surface has effectively been removed. Note that a thin basalt (<0.5 m thick) has been encountered in some wells at the aquifer/aquitard boundary. While the lateral distribution of this basalt is unknown, surprisingly there is no clear manifestation of this anomaly in the GPR or seismic amplitudes (prior to AGC), reflection traveltimes, or reflection surfaces. This suggests that the basalt is present only in isolated distributions. The mean basalt thickness is less

than uncertainty in the depths to clay and so the variability probably includes scattering from the irregular distribution of basalt.

Better velocity resolution in the GPR data and the resulting improvement in clay depth accuracy enabled a significant improvement in the seismic velocity and depth estimates. The uncertainty in depth to clay determined from the GPR and seismic interpretation is nearly equivalent (± 0.32 m for GPR and ± 0.46 m for seismic), but the wavelengths differ by a factor of greater than 4. It is surprising that the large difference in wavelengths between the seismic and GPR data was not manifest as a greater difference in uncertainty of depth to clay. This observation suggests that there is little lateral variability in the nature of the Unit 1/clay interface.

Combined 3D Interpretation

With accurate velocity and depth models for both the GPR and seismic data volumes it is now possible to derive an integrated 3D interpretation that more fully describes the hydrologic system (Figures 11 and 12). In the shallow aquifer, coherent GPR reflections are generated at the base of the Unit 5 sand channel, the Unit 4/Unit 3 boundary, and the Unit 2/Unit 1 boundary. These horizons and interpretation were discussed in greater detail by Bradford et al. (2009). Because of a gradational and irregular porosity distribution, the Unit 3/Unit 2 boundary does not produce a coherent GPR reflection, however, the porosity decrease associated with Unit 3 is manifest as a velocity increase that is well resolved through reflection tomography (Figures 2 and 5). Furthermore, the Unit 1/aquitard boundary is clearly imaged with the 50 MHz GPR data; critical to producing this high quality image was multi-fold acquisition and processing. The clay surface in the GPR appears as a relatively flat surface that begins to dip downward at the southwestern extent of the survey area.

The seismic data volume reveals that the aquitard surface continues to trend to greater depths toward the southwest. The depression roughly parallels the cross-line (X) direction of the 3D surveys (Figures 11 and 12). The depression parallels the course of the Boise River, and I interpret this feature as a paleochannel cut deeper into the clay. The base of the channel reaches a maximum depth of 23 m and is deeper than the mean clay surface by up to 5 m. This depression is a large scale feature that likely has a significant impact on flow dynamics in the shallow aquifer. Toward the northeast, the clay surface is variable but generally shallows reaching a minimum depth of just 13 m (Figures 11 and 12). The shallowest depth occurs in an area where no borehole control was available and the clay was not previously thought to reach this near to the surface at the BHRS.

There is no well control below the clay aquitard, but the seismic data provides new information that helps constrain our understanding of the deeper aquifer system. From the aquitard to a depth of 60 m, no strong reflections are present. It is unlikely that the clay aquitard is 20 m thick, so the thickness of the clay is likely below the seismic resolution. The interval from 20 – 60 m depth is associated with a substantial velocity inversion decreasing from ~2400 m/s in the surface aquifer to ~1800 m/s in the deeper interval (Figure 10). A series of lakes filled the western Snake River valley in the late Miocene-Pliocene and these lake sediments typically have a substantially higher concentration of fine grained materials than the BHRS surficial aquifer. Compressional-wave velocity tends to decrease with increasing concentration of fines (Han et al., 1986, Table 1). Therefore the velocity inversion below the aquitard is consistent with a transition to fine-grained lacustrine sediments. Note that there is of course overlap between the velocity of sand rich and fine rich materials so the interpretation is not unique.

The top of a 25 m thick unit of strong reflectivity is present at a depth of 60 m. This unit dips gently toward the northeast, and the upper and lower surfaces are nearly parallel, although the lower surface dips more steeply toward the north resulting in a thickening of the package in that direction. The deep unit is associated with an increase in velocity to 2050 m/s. In this environment, it would not be surprising to find a layer of basalt, however, the measured velocity is too low to support this interpretation. The 2050 m/s value is closer to the velocity of the alluvium found in the surface aquifer and the unit is likely comprised of coarser grained materials than the overlying low velocity unit. This deep unit may well comprise a deeper confined aquifer.

CONCLUSIONS

Despite apparently adverse conditions for surface seismic data acquisition, the BHRS proved to be a suitable environment for acquisition of high quality seismic and GPR data. Because of interference by energy scattered from surface objects, acquisition of multi-fold GPR data coupled with pre-stack dip filtering proved critical to producing a coherent image of the clay aquitard at a depth of 18 – 20 m. Similarly, the presence of a 2m high sand berm produced statics anomalies that made residual statics corrections a critical step in producing a coherent seismic data volume.

Both GPR and seismic reflection were effective for delineating the clay aquitard. Using a quantitative comparison of the clay surface interpreted from the GPR and seismic data, I was able to improve the seismic velocity estimate for the surficial aquifer by about 10% resulting in a less than 1% difference from the average velocity measured in previously analyzed vertical seismic profiles. The resulting seismic data volume provided a laterally continuous image of the clay surface over the entire well field that is within ±0.46 m of the depth-to-clay measured in

wells. Additionally, the upper and lower surfaces of what may be a 25 m thick confined aquifer at depth of 60 m. This new information provides an improved understanding of the hydrologic system at the BHRS which can be utilized in future planning, development, and research at the site.

The relatively simple quantitative integration of GPR and seismic data presented here suggests the significant advantages that can be gained where it is possible to acquire both types of data simultaneously. Additionally, utilizing shallow GPR images to develop and improve seismic statics corrections in arid environments is likely a fruitful area for future research, by improving estimates of depth to the water table for example. The complementary data provided by the seismic and GPR methods provides a rich source of information that can lead to improved site characterization.

ACKNOWLEDGEMENTS

The US Environmental Protection Agency funded this work under Grant # X-97008501-0. Boise State University acknowledges support of this research by Landmark Graphics Corporation via the Landmark University Grant Program. Graduate students Josh Nichols, Joel Brown, Dylan Mikesell, and Leah Steinbronn acquired the multi-fold GPR data. Graduate students Scott Hess, Vijaya Raghavendra, and research faculty member Bill Clement acquired the 3D seismic reflection data. Warren Barrash provided the porosity logs and insight to the BHRS geologic setting and hydrology.

REFERENCES

Annan, A.P., 2005, Ground-penetrating radar, *in* Butler, D.K., Ed., Near-Surface Geophysics: Society of Exploration Geophysicists, Investigations in Geophysics no. 13, 357-438.

Bachrach, R., and J. Rickett, 1999, Ultra shallow seismic reflection in depth: Examples

from 3D and 2D ultra shallow surveys with applications to joint seismic and GPR imaging: 69th International Meeting of the Society of Exploration Geophysicists, Society of Exploration Geophysicists.

Baker, G.S., D.W. Steeples, C. Schmeissner, M. Pavlovic, and R. Plumb, 2001, Near-surface imaging using coincident seismic and GPR data: Geophysical Research Letters, **28**, 627-630.

Barrash, W., and T. Clemo, 2002, Hierarchical geostatistics and multifacies systems: Boise Hydrogeophysical Research Site, Boise, Idaho: Water Resources Research, **38**, 1196, 10.1029/2002WR001436.

Barrash, W., T. Clemo, J.J. Fox, and T.C. Johnson, 2006, Field, laboratory, and modeling investigation of the skin effect at wells with slotted casing, Boise Hydrogeophysical Research Site: Journal of Hydrology, **326**, 181-198.

Barrash, W., T. Clemo, and M.D. Knoll, 1999, Boise Hydrogeophysical Research Site (BHRS): Objectives, design, initial geostatistical results: SAGEEP '99, Symposium on the Application of Geophysics to Environmental and Engineering Problems, Environmental and Engineering Geophysical Society, 713-722.

Barrash, W., and E.C. Reboulet, 2004, Significance of porosity for stratigraphy and textural composition in subsurface coarse fluvial deposits, Boise Hydrogeophysical Research Site: Geological Society of America Bulletin, **116**, 1509-1073, doi:10.1130/B25370.1.

Bertete-Aguirre, H., and P. Berge, 2002, Recovering soil distributions from seismic data using laboratory velocity measurements: Journal of Environmental and Engineering Geophysics, **7**, 1-10.

Bertete-Aguirre, H., P. Berge, and J.J. Roberts, 2003, A method for using laboratory measurements of electrical and mechanical properties to assist in the interpretation of field data from shallow geophysical measurements: Journal of Environmental and Engineering Geophysics, **8**, 23-29.

Bradford, J.H., W.P. Clement, and W. Barrash, 2009, Estimating porosity via ground-penetrating radar reflection tomography: A controlled 3D experiment at the Boise Hydrogeophysical Research Site: Water Resources Research, **45**, W00D26, doi:10.1029/2008WR006960.

Bradford, J.H., C.R. Johnson, T.R. Brosten, J.P. McNamara, and M.N. Gooseff, 2007, Imaging thermal stratigraphy in fresh water lakes using georadar: Geophysical Research Letters.

Cardiff, M., W. Barrash, P. Kitanidis, B. Malama, A. Revil, S. Straface, and E. Rizzo,

2009, A potential-based inversion of unconfined steadyh-state hydrologic tomography: Ground Water, **47**, 259-270.

Cardimona, S.J., W.P. Clement, and K. Kadinsky-Cade, 1998, Seismic reflection and ground-penetrating radar imaging of a shallow aquifer: Geophysics, **63**, 1310-1317.

Carmichael, R.S., 1982, Handbook of Physical Properties of Rocks, **II**, CRC Press, 345.

Chow, J., J. Angelier, J.J. Hua, J.C. Lee, and R. Sun, 2001, Paleoseismic event and active faulting: from ground penetrating radar and high-resolution seismic reflection profiles across the Chihshang Fault, eastern Taiwan: Tectonophysics, **333**, 241-259.

Clement, W.P., W. Barrash, and M.D. Knoll, 2006, Reflectivity modeling of ground penetrating radar: Geophysics, **71**, K59-K66.

Clement, W.P., and M.D. Knoll, 2006, Traveltime inversion of vertical radar profiles: Geophysics, **71**, K67-K76.

Dupuis, J.C., K.E. Butler, and A.W. Kepic, 2007, Seismoelectric imaging of the vadose zone of a sand aquifer: Geophysics, **72**, A81-A85.

Ernst, J.R., A.G. Green, H. Maurer, and K. Holliger, 2007, Application of a new 2D time-domain full-waveform inversion scheme to crosshole radar data: Geophysics, **72**, J53-J64.

Ghose, R., and E.C. Slob, 2006, Quantitative integration of seismic and GPR reflections to derive unique estimates for water saturation and porosity in subsoil: Geophysical Research Letters, **33**, L05404.

Haeni, F.P., 1996, Use of ground-penetrating radar and continuous seismic-reflection profiling on surface-water bodies in environmental and engineering studies.: J. Env. Eng. Geophys., **1**, 27-35.

Hamilton, E.L., 1971, Elastic properties of Marine Sediments: Journal of Geophysical Research, **76**, 579-604.

Han, D., A. Nur, and D. Morgan, 1986, Effects of porosity and clay content on wave velocities in sandstones: Geophysics, **51**, 2093-2107.

Heinz, J., S. Kleineidam, G. Teutsch, and T. Aigner, 2003, Heterogeneity patterns of Quaternary glaciofluvial gravel bodies (SW-Germany): Applications to hydrgeology: Sedimentary Geology, **158**, 1-23.

Imberger, J., 1985, the diurnal mixed layer: Limnology and Oceanography, **30**, 737-770.

Irving, J.D., M.D. Knoll, and R.J. Knight, 2007, Improving crosshole radar velocity tomograms: Geophysics, **72**, J31-J41.

Jardani, A., A. Revil, W. Barrash, A. Crespy, E. Rizzo, S. Straface, M. Cardiff, B. Malama, C.R. Miller, and T.C. Johnson, 2009, Reconstructrion of the water table from self-potential data during dipole pumping/injection test experiments: Ground Water, **47**, 213-227.

Johnson, T.C., P.S. Routh, W. Barrash, and M.D. Knoll, 2007, A field comparison of Fresnel zone and ray-based GPR attenuation-difference tomography for time-lapse imaging of electrically anomalous tracer or contaminant plumes: Geophysics, **72**, G21-G29.

Jussel, P., F. Stauffer, and T. Dracos, 1994, Transport modeling in hetergeneous aquifers: 1. Statistical description and numerical generation: Water Resources Research, **30**, 1803-1817.

Klingbeil, R., S. Kleineidam, U. Asprion, T. Aigner, and G. Teutsch, 1999, Relating lithofacies to hydrofacies: Outcrop-based hydrogeological characterization of Quaternary gravel deposits: Sedimentary Geology, **129**, 299-310.

Koesoemadinata, A.P., and G.A. McMechan, 2002, Correlations between seismic parameters, EM parameters, and petrophysical/petrological properties for sandstone and carbonate at low water saturations: Geophysics, **68**, 870-883.

Moret, G.J.M., W.P. Clement, M.D. Knoll, and W. Barrash, 2004, VSP traveltime inversion: Near-surface issues: Geophysics, **69**, 245-351.

Moret, G.J.M., M.D. Knoll, W. Barrash, and W.C. Clement, 2006, Investigating the stratigraphy of an alluvial aquifer using crosswell seismic traveltime tomography: Geophysics, **71**.

Mwenifumbo, C.J., W. Barrash, and M.D. Knoll, 2009, Capacitive conductivity logging and electrical stratigraphy in a high-resisitivity aquifer, Boise Hydrogeophysical Research Site: Geophysics, **74**, E125-E133.

Rashed, M., and K. Nakagawa, 2004, High-resolution shallow seismic and ground penetrating radar investigations revealing the evolution of the Uemachi Fault system, Osaka, Japan: The Island Arc, **13**, 144-156.

Ronen, J., and J.F. Claerbout, 1985, Surface-consistent residual statics estimation by stack-power maximization: Geophysics, **50**, 2759-2767.

Santamarina, J.C., V.A. Rinaldi, D. Fratta, K.A. Klein, Y.H. Wang, G.C. Cho, and G. Cascante, 2005, A survey of elastic and electromagnetic properties of near-surface soils,

in Butler, D.K., Ed., Near-Surfaced Geophysics: Society of Exploration Geophysicists, Investigations in Geophysics no. 13, 71-87.

Schwamborn, G.J., J.K. Dix, J.M. Bull, and V. Rachold, 2002, High-resolution seismic and ground penetrating radar - Geophysical profiling of a thermokarst lake in the Western Lena Delta, Northern Siberia: Permafrost and Periglacial Processes, **13**, 259-269.

Sloan, S.D., G.P. Tsoflias, D.W. Steeples, and P.D. Vincent, 2007, High-resolution ultra-shallow subsurface imaging by integrating near-surface seismic reflection and ground-penetrating radar data in the depth domain: Journal of Applied Geophysics, **62**, 281-286.

Stork, C., 1992, Reflection tomography in the postmigrated domain: Geophysics, **57**, 680-692.

Szaraneic, E., 1976, Fundamental functions for horizontally stratified earth: Geophysical Prospecting, **24**, 528-548.

Szaraneic, E., 1979, Towards unification of geophysical problems for horizontally stratified media: Geophysical Prospecting, **27**, 576-583.

Thorpe, S.A., and J.M. Brubaker, 1983, Observations of sound reflection be temperature microstructure: Limnology and Oceanography, **28**.

Ursin, B., 1983, Review of elastic and electromagnetic wave propagation in horizontally layered media: Geophysics, **48**, 1063-1081.

Wharton, R.P., G.A. Hazen, R.N. Rau, and D.L. Best, 1980, Electromagnetic propagation logging: advances in technique and interpretation: 55th Annual Fall Technical Conference and Exhibition, Society of Petroleum Engineers. Paper 9267.

TABLE CAPTIONS

Table 1. Typical velocity ranges and wavelengths for a 200 Hz seismic P-wave and a 50 MHz electromagnetic wave in common, unconsolidated near surface (low pressure) materials. No velocity is reported for the EM wave in clay as the GPR signal typically is attenuated very rapidly and does not propagate effectively in clay. Data compiled from a variety of sources including (Annan, 2005; Bertete-Aguirre and Berge, 2002; Bertete-Aguirre et al., 2003; Carmichael, 1982; Hamilton, 1971; Han et al., 1986; Santamarina et al., 2005)

Table 2. Properties of the 5 primary lithologic units at the BHRS interpreted from cores and neutron porosity logs (see Figure 2). Adapted from Barrash and Clemo (2002).

FIGURE CAPTIONS

Figure 1: Map of the BHRS showing topographic variation, well positions, 3D seismic coverage, and GPR profiles. The sand berm on the northwest side of the site created a significant statics problem. Well casings and other surface obstructions prevented true 3D GPR data acquisition.

Figure 2: Neutron porosity log from the BHRS with the five major hydrostratgraphic units defined by Barrash and Clemo (2002). Unit 5 is a medium to coarse grained sand channel, while Units 1 - 4 are comprised of poorly sorted sand, gravel, and cobbles and are differentiated primarily by porosity (Table 2). The water content derived from GPR velocity inversion approximates a running average of the porosity log and follows the large scale trends in porosity variation.

Figure 3: Representive CMPs from each of the five in-line GPR profiles. The clay reflection has a near-offset arrival time of around 450 ns and is indicated by arrows. Heavy contamination of

late arrivals by surface scatter resulted in a signal to noise ratio of less than 1 at the clay reflection.

Figure 4: A) Single-offset, conventional GPR image through the center of the well field. Reflections are interpretable to around 300 ns but the clay reflection between 450 and 500 ns is almost totally obscured by surface scatter. B) CMP stcking significantly improves the signal-to-noise ratio. C) Final stacked image after pre-stack *f-k* filtering in the CMP domain followed by CMP stacking. In the final section, all major hydrostratigraphic boundaries down to the clay aquitard are clearly imaged.

Figure 5: In-line GPR velocity model through the center of the well field produced using reflection tomography. Interpretation of the clay surface after pre-stack depth migration with this velocity model agrees with clay depths measured in the wells to within 0.03 m ± 0.3 m. The portion of the velocity model that is constrained by the full range of offsets is shown. The velocity model is clipped at 0.11 m/ns but reaches 0.15 m/ns in the vadose zone. The water table is at 2 m depth.

Figure 6: Representative shot gather A) before residual statics, and B) after residual statics. A 2 m high sand berm on the northwest side of the site (Figure 1) produced a significant statics anomaly. Residual statics were effective at improving the coherence of reflecting horizons, this is particularly evident between channels 100 – 240.

Figure 7: CMP fold map for the 3D seismic survey with well positions shown as black circles. The maximum fold is 240 and the mean fold over the entire grid is 55. The survey was designed to provide high fold near the center of the well field.

Figure 8: Representative CMP supergather after residual statics. The supergather was formed by summing traces within a 3x3 CMP bin area and was utilized for the final round of velocity analysis.

Figure 9: In-line seismic CMP stack crossing through the center of the well field showing the clay aquitard dipping toward the left and deeper reflecting horizons dipping toward the right. The surface topography is shown at the top. A) The clay surface in the stack before statics corrections is evident on the left but decreases in coherence on the right. B) After statics corrections both the clay and deeper reflections are clearly imaged across the entire profile.

Figure 10: Site averaged seismic velocity models before (start) and after (final) adjustment based on correlation of the clay interface reflection with the GPR interpretation. After adjustment, the velocity of 2417 m/s in the surface aquifer is consistent with velocity estimates from borehole measurements. The velocity of 1700 m/s below the clay interface is consistent with expected values for fine grained lake sediments.

Figure 11: Combined GPR and seismic volumes show excellent correlation of the clay interface. Note that this horizon has been shifted down by 1.5 m from the true position so that the GPR and seismic reflections are visible. The high resolution of the GPR data enable detailed interpretation of the surface aquifer stratigraphy, whereas the seismic data image deeper strata that may have significance for the underlying confined aquifer.

Figure 12: Shaded relief surface images showing the combined interpretation of all major hydrostratigraphic interfaces at the BHRS. Horizons shown in color were interpreted from the GPR data volume, and gray scale surfaces were interpreted from the 3D seismic volume.

Table 1. Typical velocity ranges and wavelengths for a 200 Hz seismic P-wave and a 50 MHz electromagnetic waves in common, unconsolidated near surface (low pressure) materials. No velocity is reported for the EM wave in clay as the GPR signal typically is attenuated very rapidly and does not propagate effectively in clay. Data compiled from a variety of sources including (Annan, 2005; Bertete-Aguirre and Berge, 2002; Bertete-Aguirre et al., 2003; Carmichael, 1982; Hamilton, 1971; Han et al., 1986; Santamarina et al., 2005)

Material	V_p (m/s)	V_{em} (m/ns)	λ_p (m) @ 200 Hz	λ_{em} (m) @ 50 MHz
Sand/gravel				
Vadose	100 – 600	0.10 – 0.16	0.5-3	2-3.2
Saturated	1700 - 3000	0.06-0.09	8.5-15	1.2-1.8
Silt				
Vadose	300-800	0.09-0.14	1.5-4	1.8-2.8
Saturated	1500-1800	0.05-0.07	8-11	1-1.4
Clay				
Vadose	300-800	--	1.5-4	--
Saturated	1500-1800	--	8-11	--
Water	1500	0.033	10	0.66

Table 2. Properties of the 5 primary lithologic units at the BHRS interpreted from cores and neutron porosity logs (see Figure 2). From Barrash and Clemo (2002)

Unit	~ Thickness	Mean Porosity	Porosity Variance	Dominant Composition
5	0 – 4 m	0.429	0.003	Coarse sand
4	1 – 5 m	0.232	0.002	Pebble/cobble dominated
3	~ 3 m	0.172	0.0006	Pebble/cobble dominated
2	~ 6 m	0.243	0.002	Pebble/cobble dominated
1	~ 2 m	0.182	0.0006	Pebble/cobble dominated

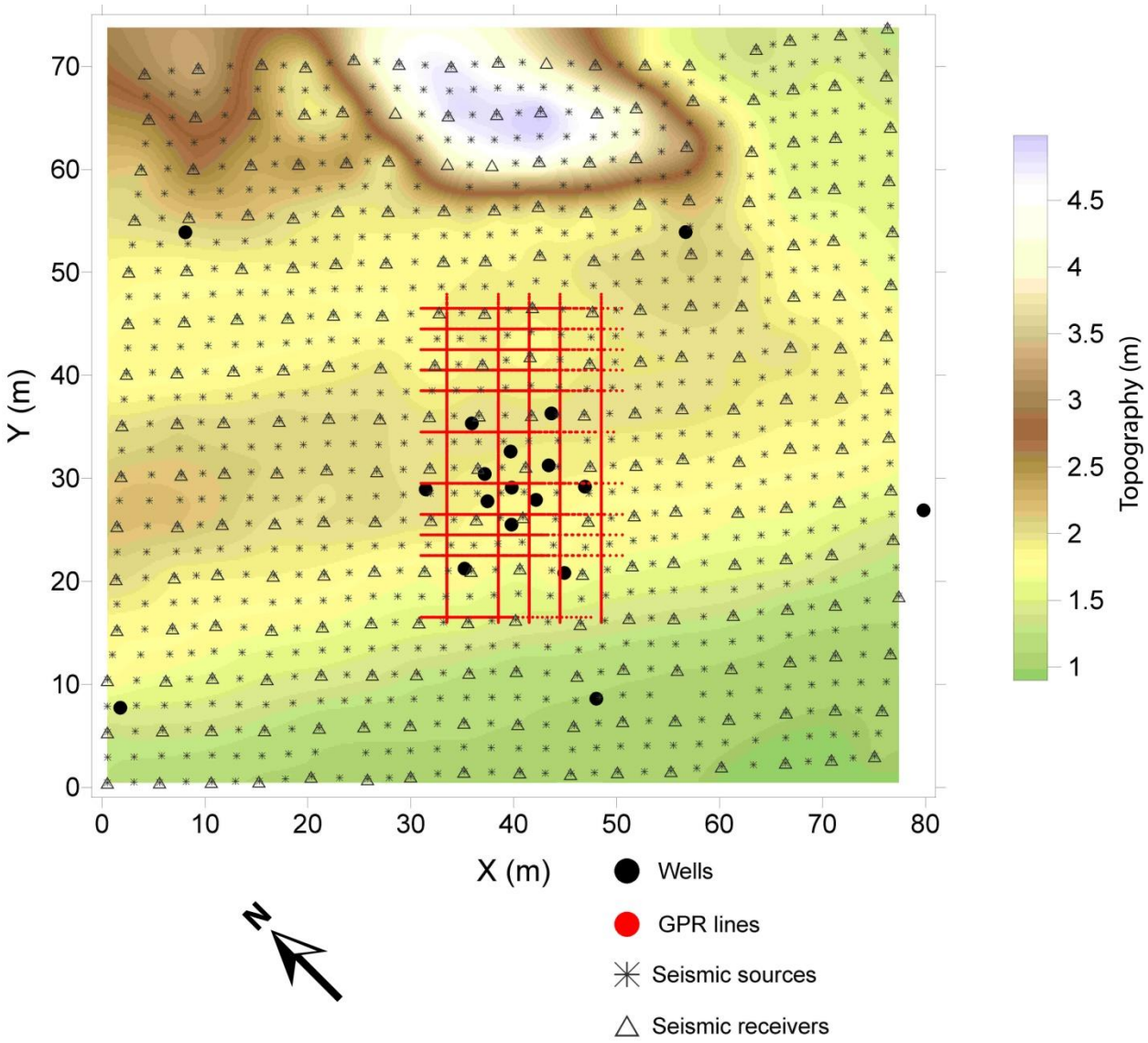

Figure 1: Map of the BHRS showing topographic variation, well positions, 3D seismic coverage, and GPR profiles. The sand berm on the northwest side of the site created a significant statics problem. Well casings and other surface obstructions prevented true 3D GPR data acquisition.

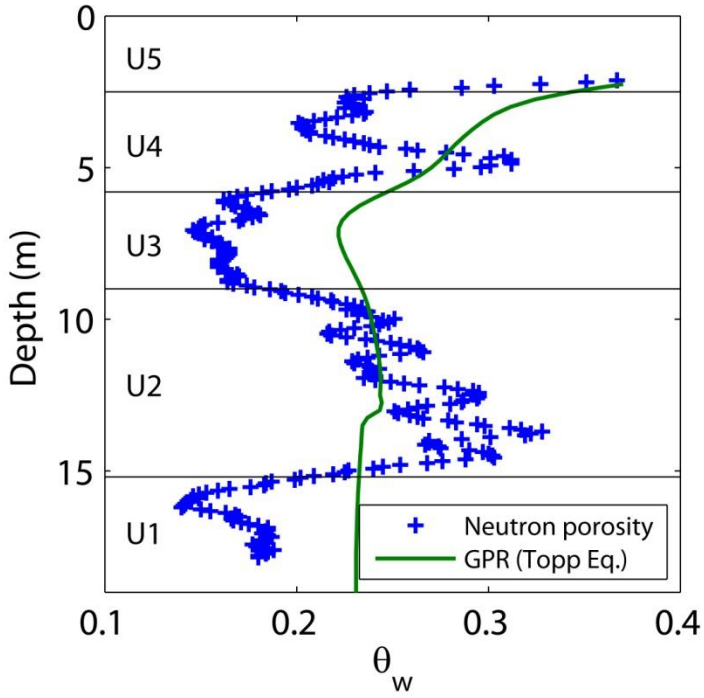

Figure 2: Neutron porosity log from the BHRS with the five major hydrostratgraphic units defined by Barrash and Clemo (2002). Unit 5 is a medium to coarse grained sand channel, while Units 1 - 4 are comprised of poorly sorted sand, gravel, and cobbles and are differentiated primarily by porosity (Table 2). The water content derived from GPR velocity inversion approximates a running average of the porosity log and follows the large scale trends in porosity

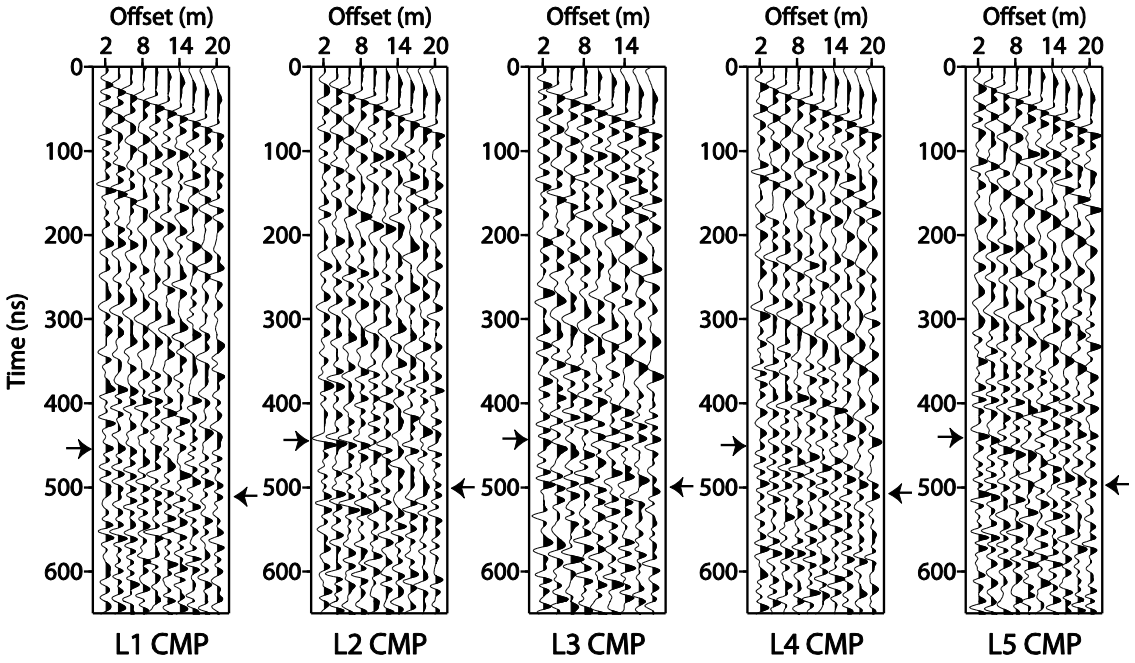

Figure 3: Representive CMPs from each of the five in-line GPR profiles. The clay reflection has a near-offset arrival time of around 450 ns and is indicated by arrows. Heavy contamination of late arrivals by surface scatter resulted in a signal to noise ratio of less than 1 at the clay reflection.

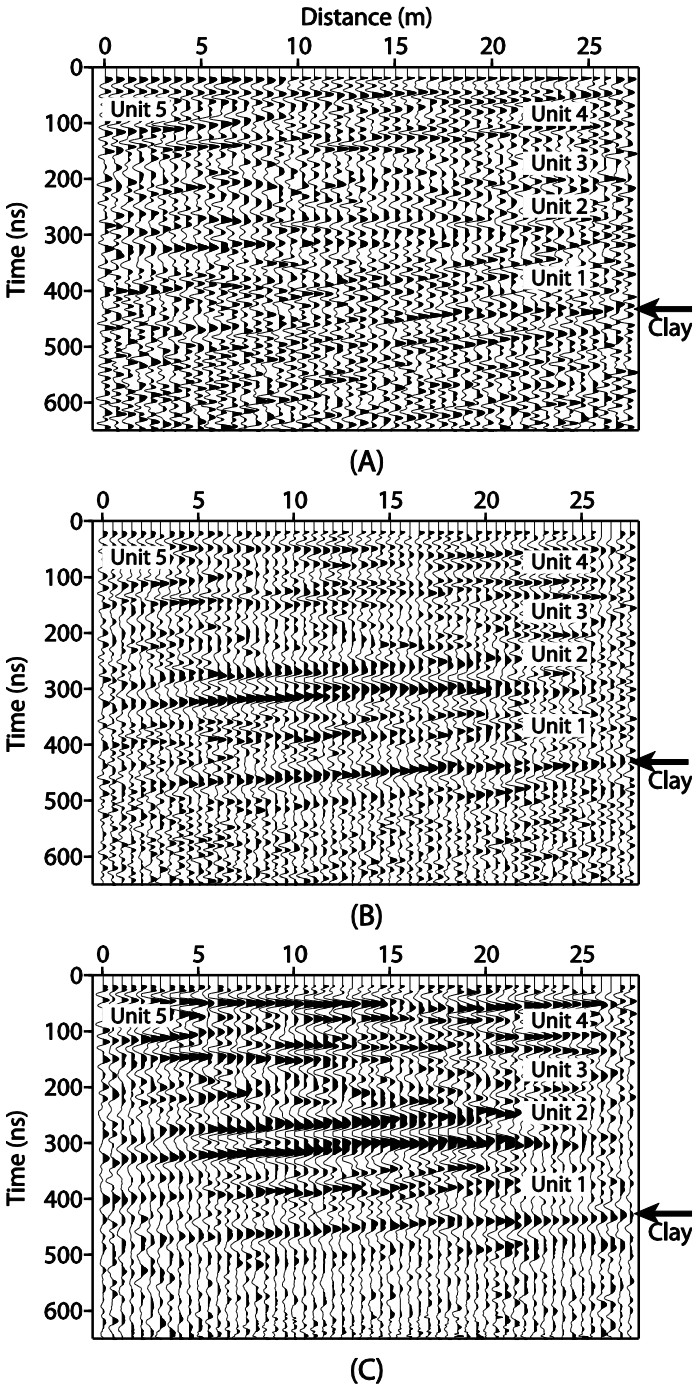

Figure 4: A) Single-offset, conventional GPR image through the center of the well field. Reflections are interpretable to around 300 ns but the clay reflection between 450 and 500 ns is almost totally obscured by surface scatter. B) CMP stcking significantly improves the signal-to-noise ratio. C) Final stacked image after pre-stack *f-k* filtering in the CMP domain followed by CMP stacking. In the final section, all major hydrostratigraphic boundaries down to the clay aquitard are clearly imaged.

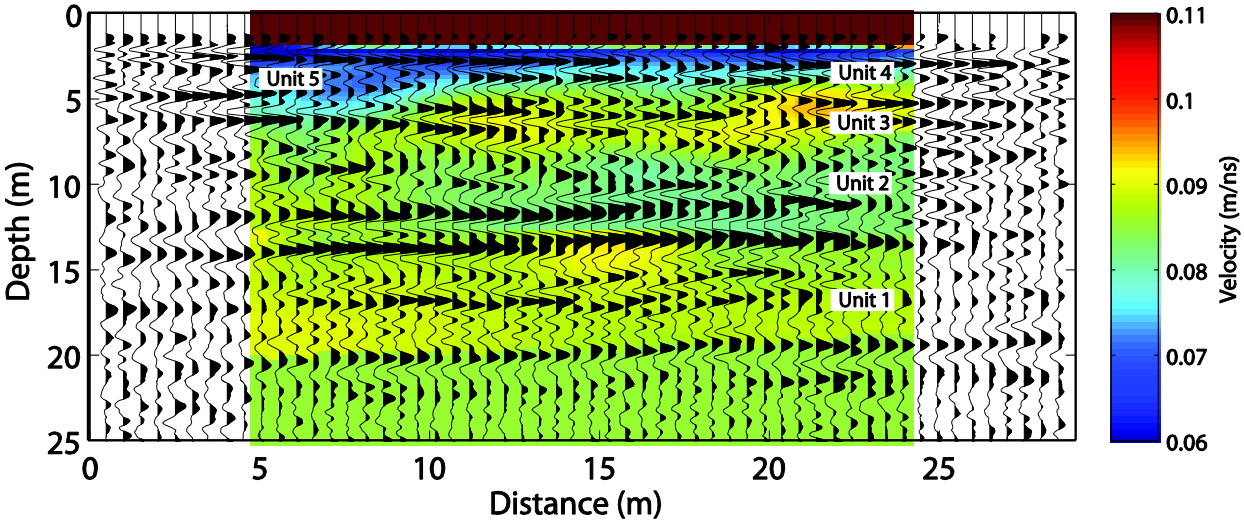

Figure 5: In-line GPR velocity model through the center of the well field produced using reflection tomography. Interpretation of the clay surface after pre-stack depth migration with this velocity model agrees with clay depths measured in the wells to within 0.03 m ± 0.3 m. The portion of the velocity model that is constrained by the full range of offsets is shown. The velocity model is clipped at 0.11 m/ns but reaches 0.15 m/ns in the vadose zone. The water table is at 2 m depth.

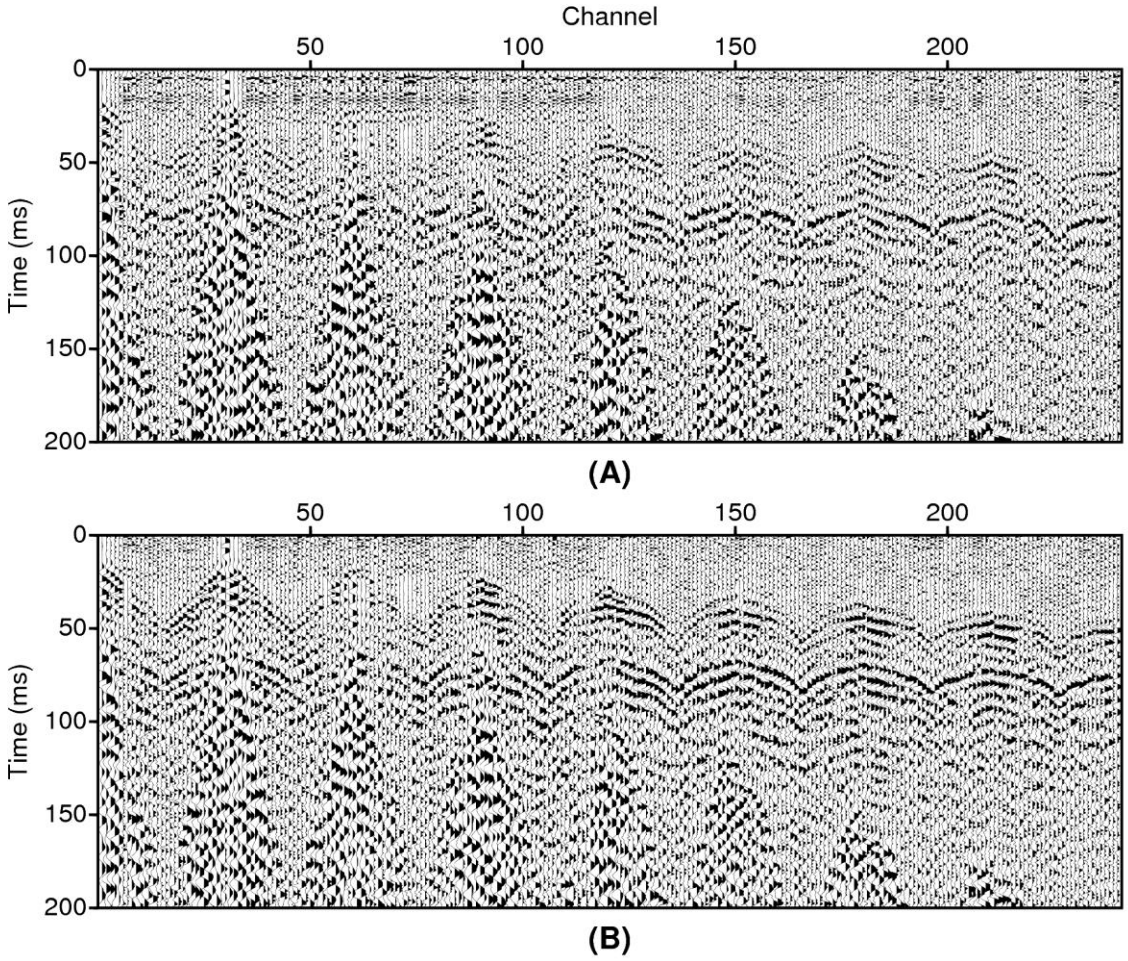

Figure 6: Representative shot gather A) before residual statics, and B) after residual statics. A 2 m high sand berm on the northwest side of the site (Figure 1) produced a significant statics anomaly. Residual statics were effective at improving the coherence of reflecting horizons, this is particularly evident between channels 100 – 240.

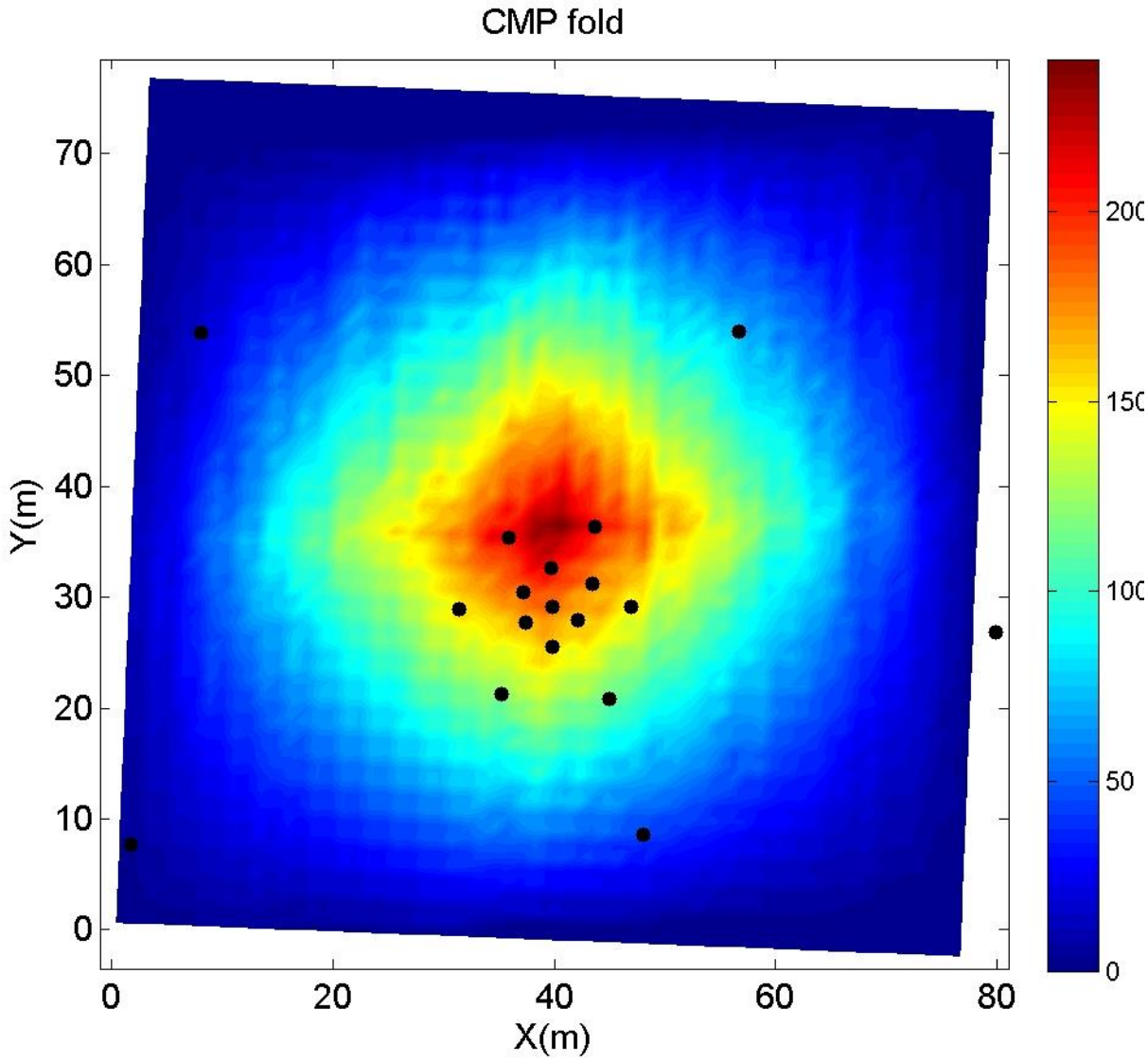

Figure 7. CMP fold map for the 3D seismic survey with well positions shown as black circles. The maximum fold is 240 and the mean fold over the entire grid is 55. The survey was designed to provide high fold near the center of the well field.

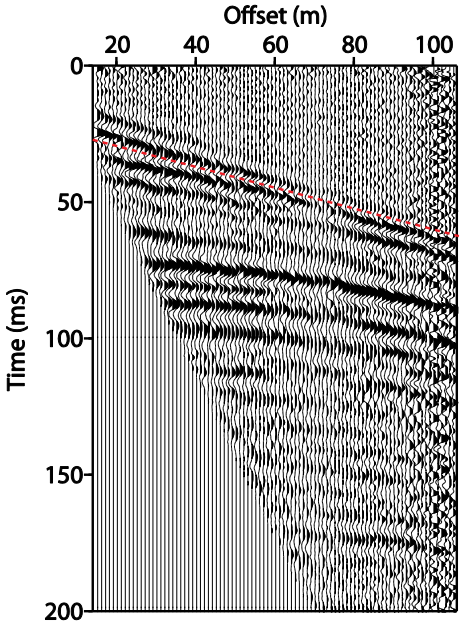

Figure 8: Representative CMP supergather after residual statics. The supergather was formed by summing traces within a 3x3 CMP bin area and was utilized for the final round of velocity analysis. All processing steps have been applied to this gather except a top mute to show the relation of the clay reflection to the water table refraction. The red dashed line shows the position of the top mute applied prior to producing the final stack. Note that the supergathers were used only for velocity analysis and that individual CMP bins were used to produce the stacked volumes.

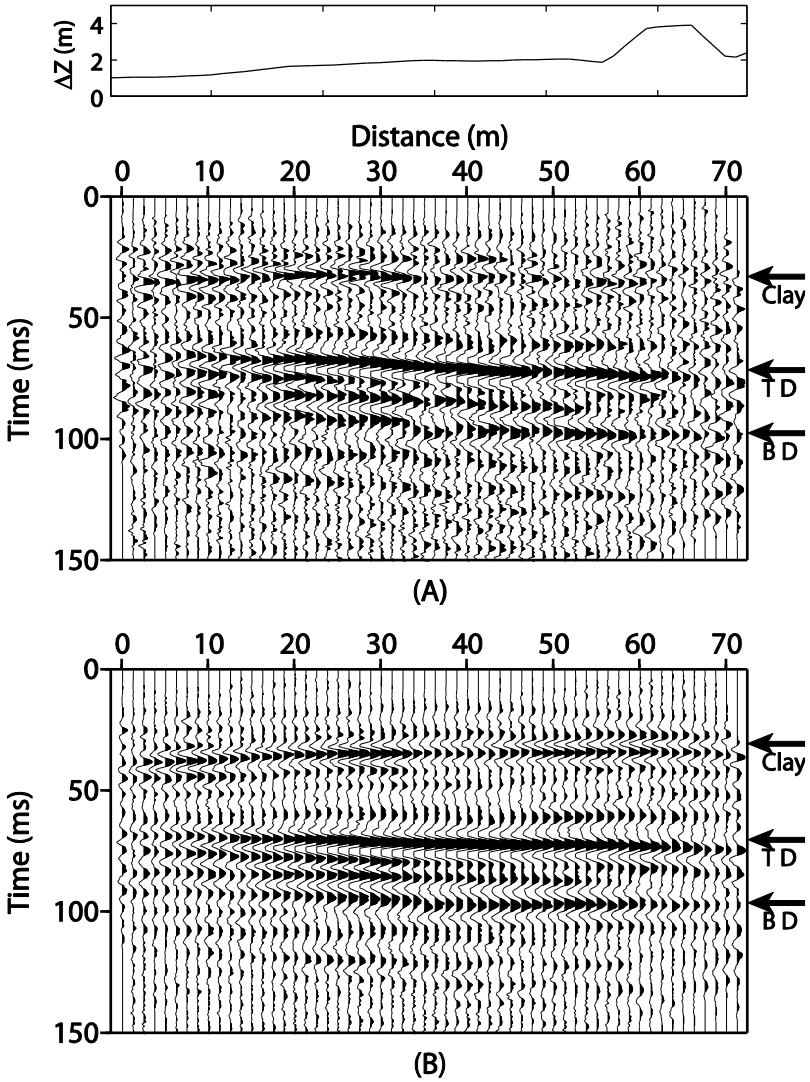

Figure 9: In-line seismic CMP stack crossing through the center of the well field showing the clay aquitard dipping toward the left and deeper reflecting horizons dipping toward the right. The surface topography is shown at the top. A) The clay surface in the stack before statics corrections is evident on the left but decreases in coherence on the right. B) After statics corrections both the clay and deeper reflections are clearly imaged across the entire profile.

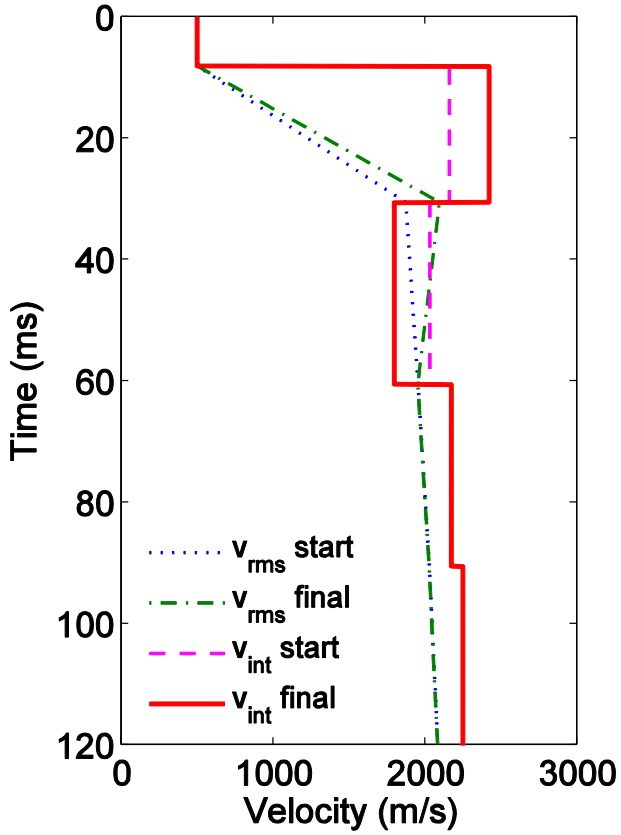

Figure 10: Site averaged seismic velocity models before (start) and after (final) adjustment based on correlation of the clay interface reflection with the GPR interpretation. After adjustment, the velocity of 2417 m/s in the surface aquifer is consistent with velocity estimates from borehole measurements. The velocity of 1800 m/s below the clay interface is consistent with expected values for fine-grained lake sediments.

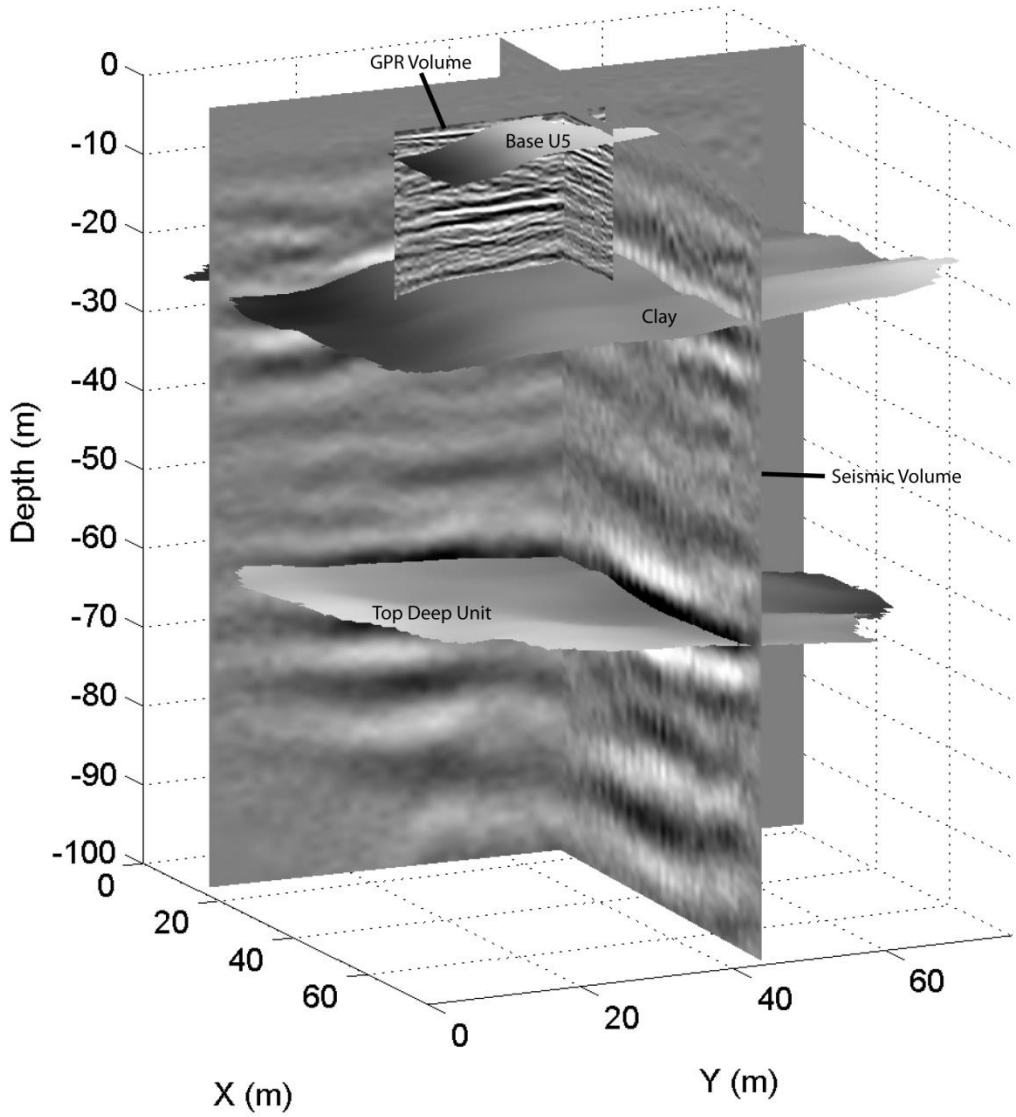

Figure 11: Combined GPR and seismic volumes show excellent correlation of the clay interface. Note that this horizon has been shifted down by 1.5 m from the true position so that the GPR and seismic reflections are visible. The high resolution of the GPR data enable detailed interpretation of the surface aquifer stratigraphy, whereas the seismic data image deeper strata that may have significance for the underlying confined aquifer.

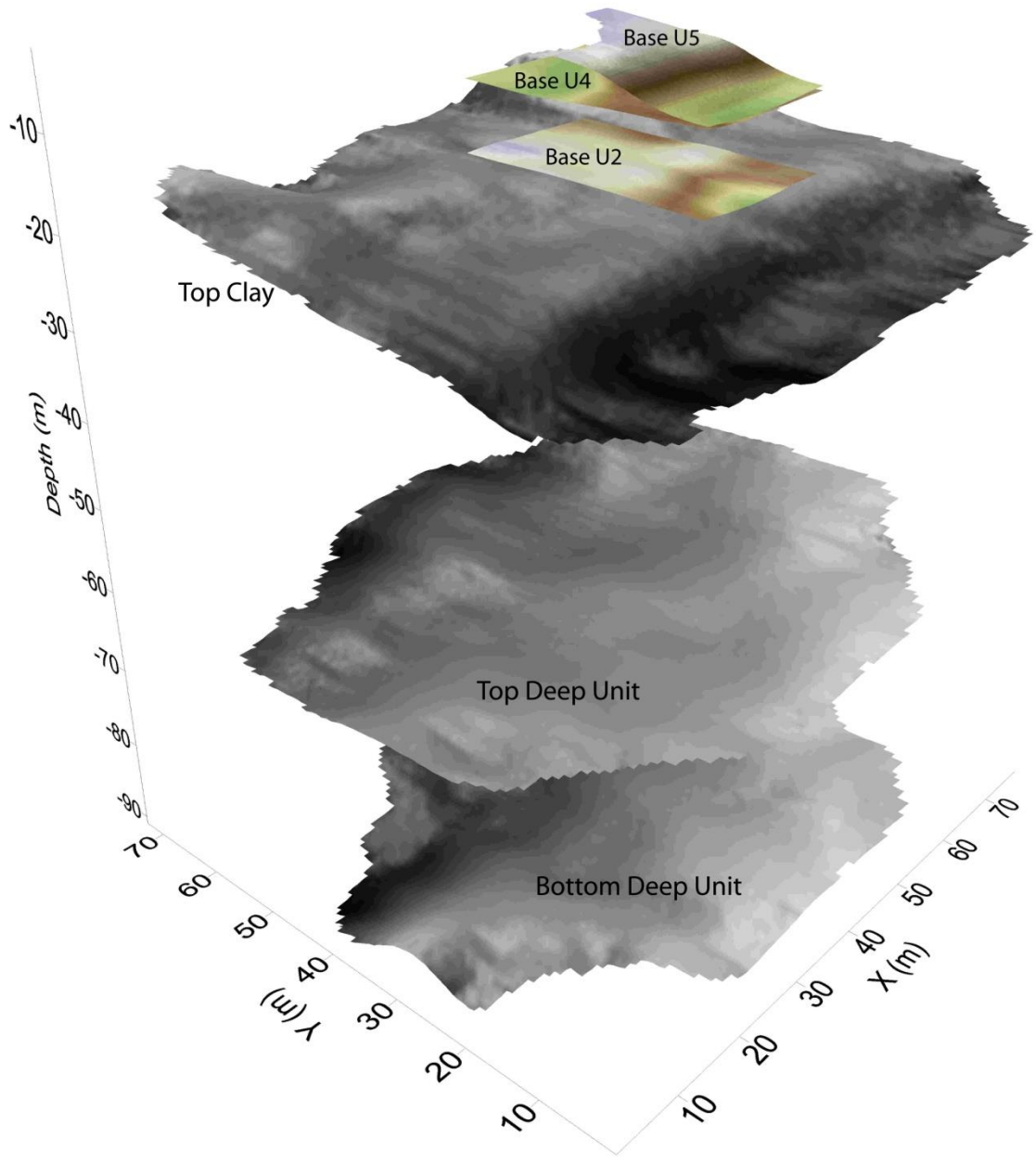

Figure 12: Shaded relief surface images showing the combined interpretation of all major hydrostratigraphic interfaces at the BHRS. Horizons shown in color were interpreted from the GPR data volume, and gray scale surfaces were interpreted from the 3D seismic volume.